

LA-UR-16-27197

Approved for public release; distribution is unlimited.

Title: Estimation of Metal Strength at Very High Rates Using Free-Surface Richtmyer-Meshkov Instabilities

Author(s): Prime, Michael Bruce; Buttler, William Tillman; Buechler, Miles Allen; Denissen, Nicholas Allen; Kenamond, Mark Andrew; Mariam, Fesseha Gebre; Oro, David Michael; Schmidt, Derek William; Martinez, John Israel; Stone, Joseph B; Tupa, Dale; McNeil, Wendy Vogan

Intended for: Journal of Dynamic Behavior of Materials

Issued: 2016-09-21

Prime MB, Buttler WT, Buechler MA, Denissen NA, Kenamond MA, Mariam FG, Martinez JI, Oró DM, Schmidt DW, Stone JB, Tupa D, Vogan-McNeil W (2017) Estimation of Metal Strength at Very High Rates Using Free-Surface Richtmyer–Meshkov Instabilities. Journal of Dynamic Behavior of Materials, Vol 3, pp. 189-202. doi:10.1007/s40870-017-0103-9.

<http://link.springer.com/article/10.1007%2Fs40870-017-0103-9>

Disclaimer:

Los Alamos National Laboratory, an affirmative action/equal opportunity employer, is operated by the Los Alamos National Security, LLC for the National Nuclear Security Administration of the U.S. Department of Energy under contract DE-AC52-06NA25396. By approving this article, the publisher recognizes that the U.S. Government retains nonexclusive, royalty-free license to publish or reproduce the published form of this contribution, or to allow others to do so, for U.S. Government purposes. Los Alamos National Laboratory requests that the publisher identify this article as work performed under the auspices of the U.S. Department of Energy. Los Alamos National Laboratory strongly supports academic freedom and a researcher's right to publish; as an institution, however, the Laboratory does not endorse the viewpoint of a publication or guarantee its technical correctness.

Estimation of Metal Strength at Very High Rates Using Free-Surface Richtmyer-Meshkov Instabilities

Michael B. Prime, William T. Buttler,
Miles A. Buechler, Nicholas A. Denissen, Mark A. Kenamond, Fesseha G. Mariam, John I. Martinez,
David M. Oró, Derek W. Schmidt, Joseph B. Stone, Dale Tupa, Wendy Vogan-McNeil

Los Alamos National Laboratory, Los Alamos, NM 87545 USA

Abstract

Recently, Richtmyer-Meshkov Instabilities (RMI) have been proposed for studying the average strength at strain rates up to at least $10^7/s$. RMI experiments involve shocking a metal interface that has initial sinusoidal perturbations. The perturbations invert and grow subsequent to shock and may arrest because of strength effects. In this work we present new RMI experiments and data on a copper target that had five regions with different perturbation amplitudes on the free surface opposite the shock. We estimate the high-rate, low-pressure copper strength by comparing experimental data with Lagrangian numerical simulations. From a detailed computational study we find that mesh convergence must be carefully addressed to accurately compare with experiments, and numerical viscosity has a strong influence on convergence. We also find that modeling the as-built perturbation geometry rather than the nominal makes a significant difference. Because of the confounding effect of tensile damage on total spike growth, which has previously been used as the metric for estimating strength, we instead use a new strength metric: the peak velocity during spike growth. This new metric also allows us to analyze a broader set of experimental results that are sensitive to strength because some larger initial perturbations grow unstably to failure and so do not have a finite total spike growth.

1 Introduction

Researchers have long used Rayleigh Taylor (RT) instabilities to infer material strength [1-3] and more recently to help develop sophisticated strength models for the high-pressure, high-rate regimes accessed in such experiments [4,5]. Fig. 1 illustrates a typical RT experiment, in which gaseous detonation products from a high explosive (HE) expand across a vacuum gap and shocklessly accelerate a sample that has initial geometric perturbations. Strength, meaning resistance to deviatoric, i.e., shear, deformation moderates the growth rates of the instabilities. The perturbation growth rates, measured experimentally with radiography, are then used to indirectly estimate the strength of the sample at very high strain rates.

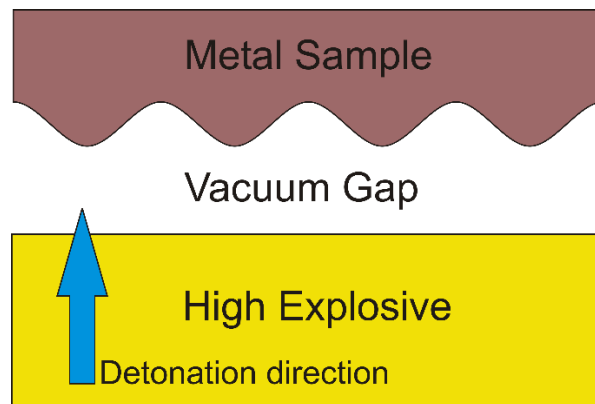


Fig. 1 Schematic of Rayleigh-Taylor instability experiment used to determine strength. The HE detonation products *shocklessly* accelerate the perturbed surface of the sample

Only more recently, researchers have shown that Richtmyer-Meshkov Instabilities (RMI) are sensitive to strength at strain rates up to at least $10^7/s$ [6-16]. Fig. 2 illustrates an RMI experiment in the configuration fielded for recent experiments [8,9]. A shock drives the RMI experiments in contrast to the RT experiments, which undergo shockless acceleration. As shown in Fig. 2, in an RMI experiment

the initial perturbations invert after shock, and the subsequent peaks are called spikes and the valleys are called bubbles. In RMI experiments, strength is usually determined by measuring total spike growth for perturbations [9,7], as compared to the growth rate metric used in RT experiments. A drawback of the total spike growth metric is that it can only be employed when strength arrests the instability growth.

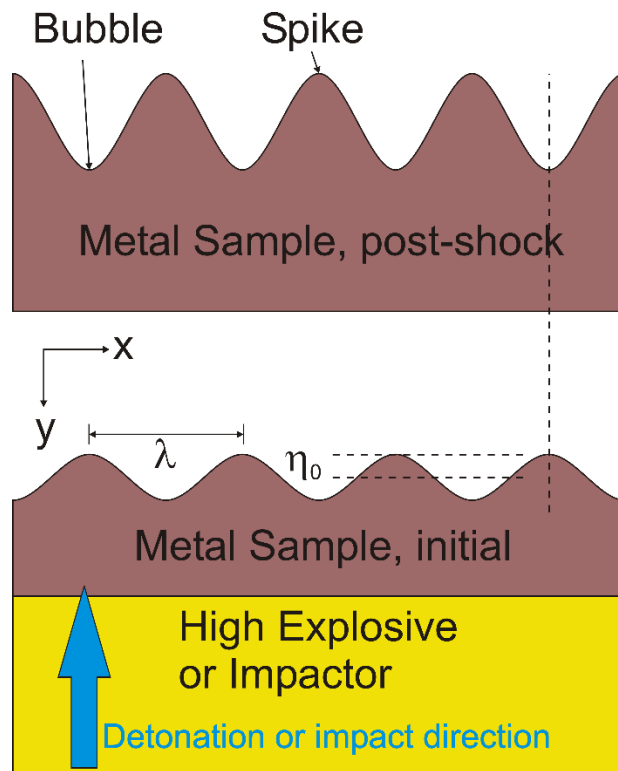


Fig. 2 Schematic of a Richtmyer-Meshkov instability experiment (for Atwood = -1). The perturbed surface of the sample is accelerated by a *shock* from an impact or from HE detonation. At later time, the perturbations have inverted

Fig. 2 shows an RMI experiment for the case of the perturbations on the free surface opposite of the shock loading (Atwood number $A = -1$). Piriz originally proposed RMI strength measurements where the perturbations were an inner surface in the experiment ($A = +1$) [6,7], following the more traditional fluid mechanics view of RMI, but such internal perturbations are difficult to experimentally field and diagnose. Most published experimental implementations of RMI for strength measurements

use the free surface configuration [8,9,17,18] partly because the free surface allows easier diagnostic access but also because free-surface experiments study the question of ejecta from a shocked surface [9,17,19-23]. Note that in the configuration of Fig. 2 the shock releases quickly from the free surface, so most of the spike growth and arrest occurs at low pressure.

In this paper, we present the most comprehensive experimental/numerical study to date on determining strength from RMI experiments, based on the approach described in Section 2. In Section 3, we present new RMI experiments on copper, with five perturbations. In Section 4, we describe the Lagrangian hydrodynamic modeling we use to analyze the data and estimate material strength. Here we use two codes for the modeling to verify some aspects of the calculations. Because the free-surface configuration causes tensile stresses relatively early, we numerically study the effects of tensile damage on the instability growth and arrest, which has not been considered before. Because of the confounding effect of damage on the traditional strength-related metric of total spike growth, we use a new metric: the peak velocity of the spike. This new metric also allows us to analyze the broader set of experimental results including experiments with larger initial perturbations that do not arrest. Previous analyses of the copper RMI data considered only a single perturbation size at a time [8,9,13,24], but we analyze five perturbation sizes. Simultaneously analyzing this broader set of data forced us to improve aspects of previous analyses and led to a more robust estimate of strength and to ideas to improve future experiments.

2 Approach

Buttler [9] presents RMI theory and equations based on Piriz's assumptions [6] in greater detail, and we adopt the same nomenclature in Fig. 2. The initial perturbation height is $\eta(x) = \eta_0 \sin(kx)$, where

$k = 2\pi/\lambda$ is the wavenumber, λ is the perturbation wavelength, and η_0 is the initial perturbation amplitude. Perturbation sizes are compared in terms of the non-dimensional amplitude-wavenumber product $\eta_0 k$. Buttler and others take the spike velocity $\dot{\eta}^s(x,t)$ as relative to the free-surface velocity measured in a perturbation-free region of the sample. Here we analyze the data independent of the free-surface velocity and call the absolute spike velocity $v^s(x,t)$.

We build on previous work [6-9,24] to estimating strength. Strength in metals varies with strain, strain rate, temperature and pressure, all of which vary temporally and spatially during an RMI experiment. Rather than attempt to solve an inverse problem to identify such dependencies of the strength behavior, we follow the literature and estimate the best-match, constant strength Y . To find the best-match Y over the full range of experimental $\eta_0 k$'s, which has not been done before, we compute the peak spike velocity for a given Y for all of the data and then calculate errors between the measured and computed values. We repeat the calculations for different values of Y and find the value that minimizes the error.

3 Experiment

The new experiment reported here is virtually identical to an experiment reported in detail previously [9,17]. The experiment approximated the ideal conditions illustrated in Fig. 2 using a plane wave lens, PBX 9501 high explosive, and a momentum trapping target. The experiment achieved a shock breakout pressure of about 36 GPa at the copper free surface [9]. The experiment was diagnosed using proton radiography [25] and Photon Doppler Velocimetry (PDV) [26-30]. The 8-mm thick 94-mm diameter target of OFHC Cu in the half-hard state with grain size of about 20 μm had bands of 550 μm wavelength perturbations eight wavelengths wide separated by flat regions 5 mm wide. The

perturbation bands were straight, running from edge to edge of the target, rather than concentric. Five initial perturbation amplitudes were fielded, $\eta_0 = 30\text{-}54 \mu\text{m}$, to give η_{ok} of 0.34, 0.39, 0.43, 0.53 and 0.62. We chose these η_{ok} 's to better constrain the previous results [9,17], where $\eta_{ok} = 0.35$ had arrested spike growth, but the next bigger η_{ok} , 0.75 had unstable spike growth.

The PDV laser light from the target was collimated to a typical diameter of about 1 mm, on the order of 2 perturbation wavelengths. When fielded in this configuration, i.e. when observing the perturbation region of the target and the subsequent bubble and spike growth, there will be a broad range of Doppler-shifted frequencies in the reflected light. These Doppler-shifted signals were heterodyned with the reference beam to give a wide spectrum of coincident beat frequencies. By computing the Fourier transform of the digitized beat frequencies, multiple velocities were resolved at once.

Dimensional inspection revealed that the as-built perturbations deviated significantly from perfect sine waves. Fig. 3 shows inspection data taken using a Zygo NewView 7300 white light interferometer and a $4.3 \mu\text{m}$ pixel size. The tops are clipped off but otherwise the shapes match a sine wave. We characterize this as-built geometry using a quality factor q , defined as

$$q = \frac{h}{2\eta_0}, \quad (1)$$

where h is illustrated in Fig. 3. $q = 1$ would be a complete sine wave and $q = 0$ would be a flat surface. The values for all geometric parameters and accompanying uncertainties were determined by fitting the inspection data and are reported later in this paper along with experimental results. The values of q ranged from 0.47 to 0.76. Because inspection data was not available for most of the previous set of

experiments [9], which were fabricated similarly, the reliability of the strength analyses in previous publications [9,8,13,24] is uncertain.

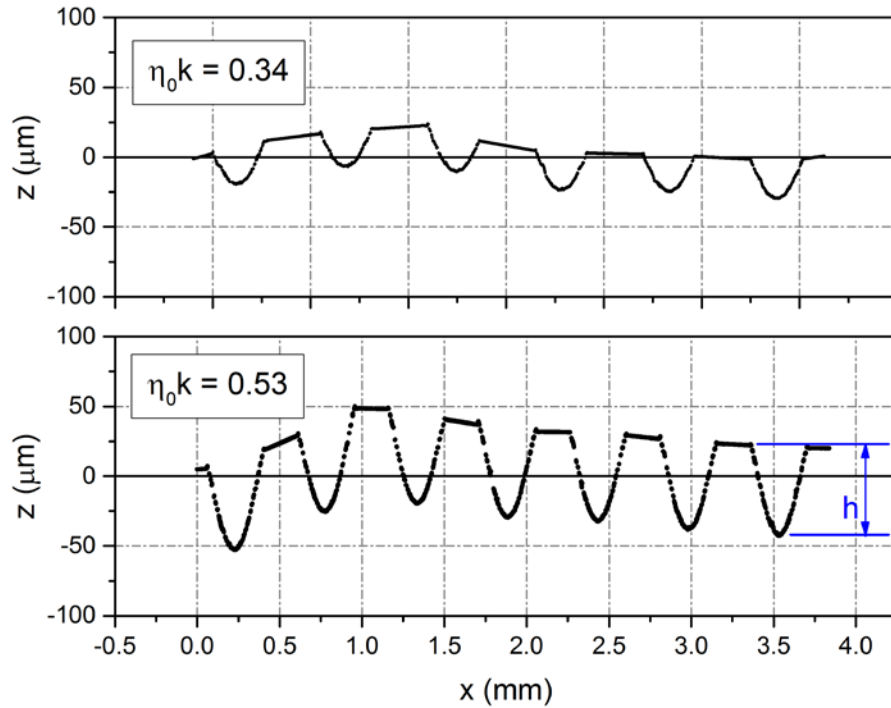


Fig. 3 Typical inspection data shows that the machined sine wave perturbations had the tops clipped off. $\eta_0 k = 0.34$ had the least complete sine waves and $\eta_0 k = 0.53$ had more complete sine waves. Note that the z -scale is magnified 1000 times relative to the x -scale

4 Modeling

We modeled the RMI experiments using FLAG, an Arbitrary Lagrangian/Eulerian, explicit, finite-volume hydrodynamics code using arbitrary polyhedral computational zones (elements) [31-35], which has been used for modeling many physical phenomena [36-40]. To understand some perplexing early results, we repeated some simulations using Abaqus Explicit [41], a Lagrangian finite element code. No mesh relaxation or Eulerian remapping was used in either software because the deformations are

modest since many of the spikes arrest in these RMI experiments, and we are only interested in the behavior early in the deformation as we will show in Section 5.2. Each simulation used a two-dimensional plane strain mesh that included two full wavelengths of the perturbation, see Fig. 4, and had constraints on the top and bottom to prevent vertical displacements, effectively assuming periodic behavior, which was reasonable for the central region of each perturbation band in the experiment. Considering the cyclic symmetry, it was not necessary to include 2 full wavelengths in the reduced model, but we wanted to make sure that the symmetry conditions did not numerically perturb the solution.

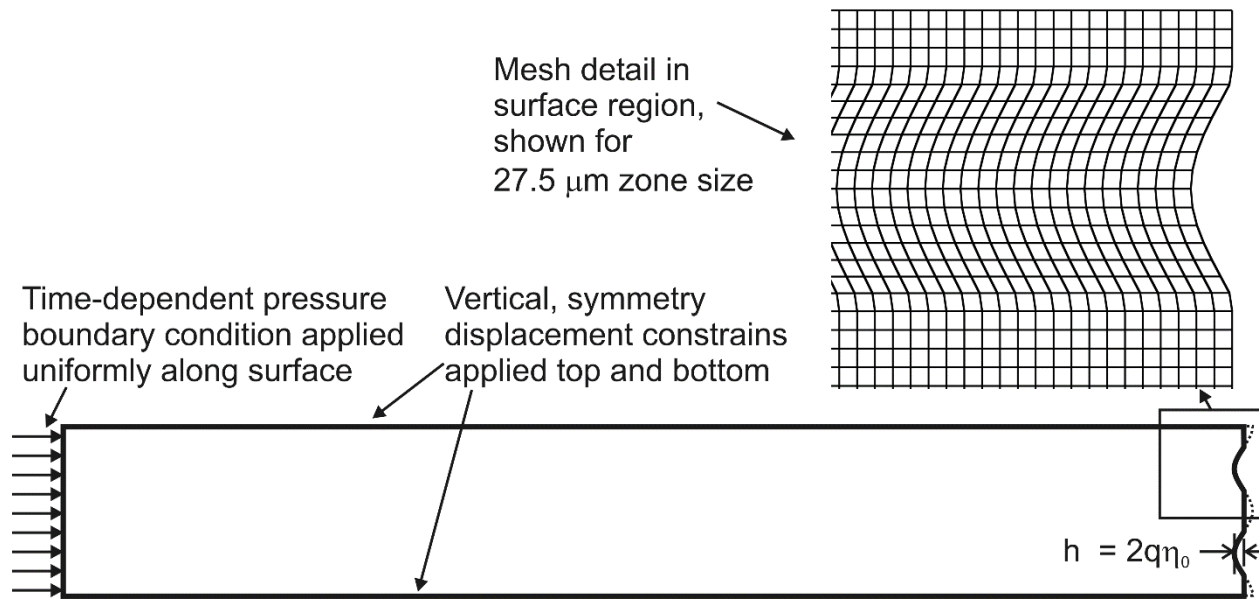


Fig. 4 The model simulated two full periods of the incomplete sine wave perturbation using Cartesian 2D plane strain computational zones (elements). Perturbation amplitude not to scale

Numerical viscosity is necessary to add entropy and correctly numerically model a shock. It also turns out to have significant impact on RMI modeling. Abaqus Explicit uses a classic VonNeumann and Richtmyer (VNR) approach [41] that adds pressure terms to the momentum equation that are linear [42] and quadratic [43] in the rate of volume change for a zone. In multi-dimensional simulations, VNR

is isotropic, i.e., viscous forces act as pressures, and the VNR viscosity vanishes for isochoric (incompressible) flows. FLAG is designed to model more complex, multi-dimensional shock-dominated problems, where VNR has drawbacks, and by default it uses a “Barton” viscosity approach [44,35] that accounts for the direction of both the flow and the shock by calculating viscosity differences and viscous forces on an edge-by-edge basis in each computational zone and applying the force in the flow direction. The Barton approach also includes linear and quadratic terms in velocity. To minimize the influence of noise and ringing, we adjusted numerical viscosities to damp out most of the artificial shock ringing without noticeably reducing the peaks in the velocity transients. The quadratic bulk viscosity parameters were set at 1.35 for both codes (coincidental since they are not comparable parameters), and the linear parameter was set at 0.2 for Abaqus and 0.3 for FLAG to achieve similar results. We were also able to run a VNR model in FLAG and isolate the impact of artificial viscosity treatments from other differences between the two codes.

We meshed the computational domain using 4-node zones with aspect ratios of approximately one as shown in Fig. 4. The final models used to estimate strength for each η_{0k} matched the as-built geometry shown in Fig. 3, but some preliminary calculations discussed below were performed prior to the inspection data and modeled a complete $q = 1$ sine wave. We selected zone sizes to have an integral number of zones within each half-wavelength of the perturbation in order to extract nodal velocities precisely at tips of the spikes and bubbles. The largest such zone size was 55 μm , giving 20 zones across the two-wavelength domain. We sequentially halved the mesh size four times for convergence studies down to a minimum zone size of $3^{7/16}$ μm for 320 zones across the domain.

We modeled the volumetric behavior of copper using a Mie-Grünesien equation of state with a reference density of 8.93 g/cm^3 , an initial Grünesien gamma, called γ_0 , of 2.02, and a linear U_s-U_p

relation $U_s = C_0 + SU_p$ with $C_0 = 0.394$ cm/ μ s and $S = 1.489$ [45]. Material temperature was calculated using the equation of state and also included heating from plastic work. As described in Section 2, we used a constant strength model to estimate the average strength value that best matched the data. Since temperatures do not affect the constant strength model, temperatures are reported for information purposes only.

To assess the impact of tensile-stress-induced damage on the experiments and data interpretation, we used an advanced damage model available in FLAG but not Abaqus. The Tonks damage model [46-49] had been previously calibrated for Cu using flyer plate spall data and, notably, incipient spall data with experimentally measured distributions of porosity [50]. For the damage calculations, the Tonks damage model was coupled with a Preston-Tonks-Wallace (PTW) deviatoric strength model [51], which was calibrated using quasi-static and Hopkinson bar stress-strain data taken at rates from 10^{-3} /s to 4300/s and temperatures from 77 K to 873 K .

In previous FLAG simulations of these experiments, we explicitly modeled the 9501 high explosive using a JWL equation of state with constants from Dobratz [52]. Using the length of the high explosive as an adjustable parameter to account for lateral and backwards constraint effects not captured by the reduced, periodic model, those simulations closely matched experimental velocities measured on regions of the target that were free from perturbations [13]. The four velocities measured on the nominally identical flat regions vary within ± 25 m/s of their average, or less than 2%, to give an idea of the uncertainty of the drive. Because the decay of the triangle wave pressure pulse is sensitive to material strength which affects the planar sound speed, we performed a further set of calculations to calibrate the loading to the constant strength, Y . To reduce simulation time, we extracted the pressure time history at the explosive-metal interface from those simulations and used

that to specify the time history of a pressure boundary condition applied uniformly to the left edge of the copper in the model. The pressure P in GPa is given as a function of the time t in microseconds by

$$P = \left(-0.00968 \left(\frac{Y}{860} \right)^2 + 0.0798 \left(\frac{Y}{860} \right) + 0.930 \right) \left(-1.5358t^5 + 12.9818t^4 - 44.8938t^3 + 83.8841t^2 - 93.6911t + 58.6794 \right), 0 < t < 2.5$$

(2)

Where Y is strength in MPa and the strength-correction term in the first set of parentheses varies from 0.94 to 1.01 for the range of Y examined in this work. Because of slight differences in the Abaqus Explicit solver accumulating over the 8 mm thickness that the shock travels in the copper, we also had to increase the pressure profile by a constant 2% in order to achieve an identical pressure drive to FLAG in the region of the perturbations.

5 Results & Discussion

5.1 Experimental Results

Fig. 5 and Fig. 6 show PDV spectrograms chosen to exemplify different aspects of the full data set. The higher velocities in each spectrogram come from the spikes and lower velocities come from bubbles or intermediate regions. The dominant late time velocity of about 1500 m/s matches the measurements taken in the flat regions of the target and is called the free-surface velocity [9]. The velocity spectrogram in Fig. 5 for $\eta_{ok} = 0.433$ shows a spike velocity that returned to the free-surface velocity about 0.6 μ s after shock breakout, indicating spike arrest. The spike velocity is quite distinct allowing easy identification of the peak, v_{\max}^s , of 2260 m/s. Fig. 6 shows a spectrogram for $\eta_{ok} = 0.621$, which has the least distinct velocity trace for the spike leading to increased uncertainty in the

estimated peak velocity of 2730 m/s peak velocity. The spike velocity trace, indicated in the inset figure is difficult to distinguish with Fig. 6 plotted on the same scale as Fig. 5 but was carefully confirmed by varying settings in the Fourier transform of the PDV data to identify and confirm the consistent presence of that feature. The spike velocity pulls back partially, indicating strength effects, but does not return to the free-surface velocity, indicating unstable growth that will continue and eventually lead to the spikes separating from the target.

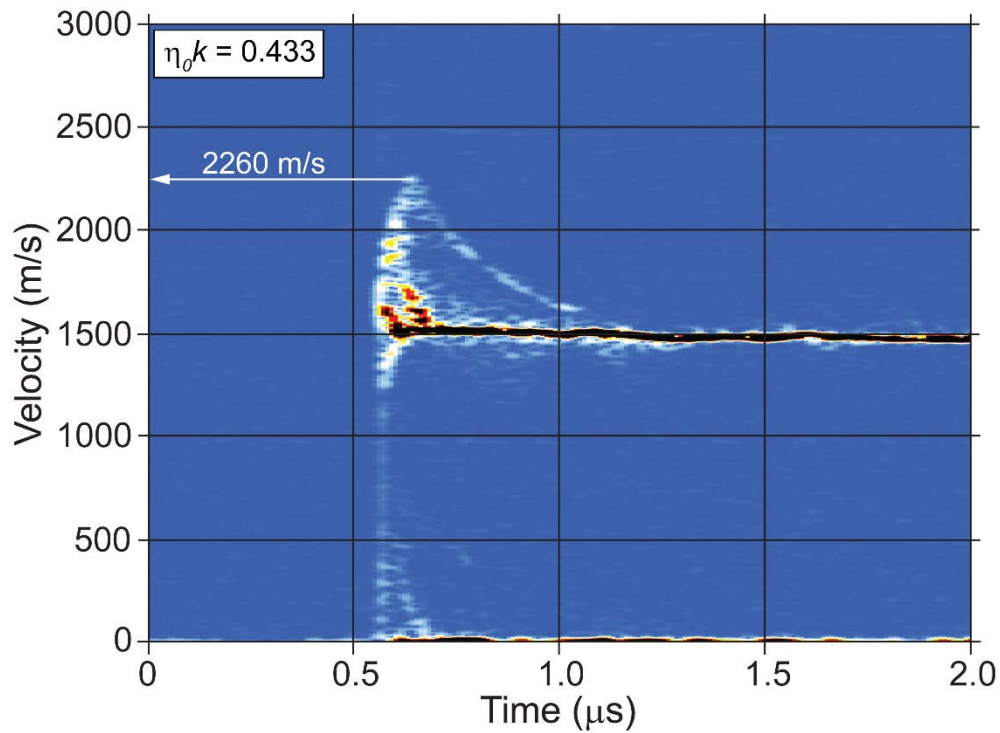


Fig. 5 The PDV velocity spectrogram for $\eta_0 k = 0.433$ shows a distinct velocity trace for the spike growth peaking at 2260 m/s. In this case, the spike velocity returned to the free-surface velocity of 1500 m/s, indicating arrest

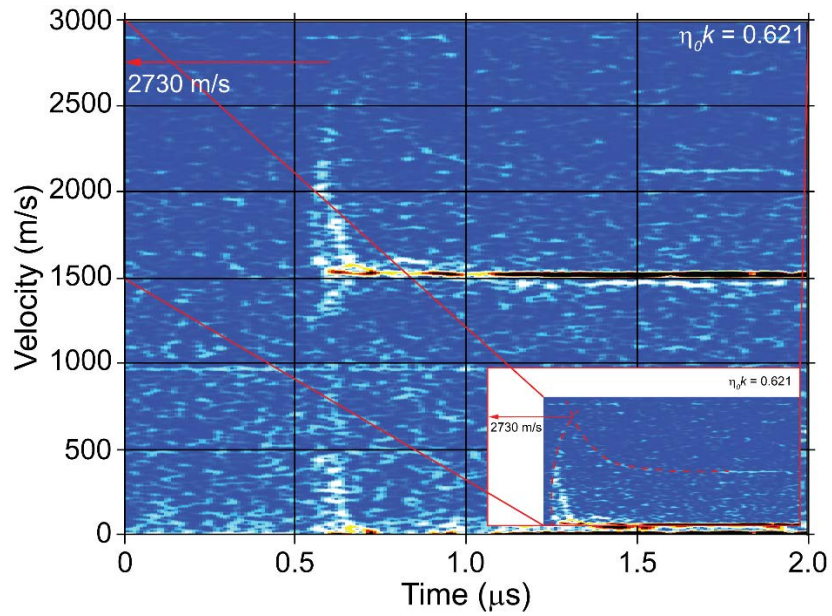


Fig. 6 The PDV Velocity spectrogram for $\eta_0 k = 0.621$ had the least distinct velocity trace for the spike with the peak estimated at 2730 m/s. The spike velocity pulls back only partially, indicating unstable growth that will continue and eventually lead to the spikes separating from the target

Table 1 summarizes the experimental results. The three smaller perturbation sizes fully arrested as observed by velocity signals like Fig. 5. The next two perturbation sizes showed strength effects but not arrest, like Fig. 6. We estimated the peak spike velocity and uncertainties manually from the PDV velocity spectrograms.

η_{0k}	Sine wave completeness, q	Behavior	Peak spike velocity (m/s)
0.344 ± 0.005	0.47 ± 0.01	Growth and arrest	2030 ± 20
0.387 ± 0.003	0.55 ± 0.01	Growth and arrest	2130 ± 20
0.433 ± 0.006	0.60 ± 0.01	Growth and arrest	2260 ± 25
0.532 ± 0.003	0.67 ± 0.01	Velocity pullback but no arrest	2510 ± 25
0.621 ± 0.015	0.76 ± 0.01	Velocity pullback but no arrest	2730 ± 30

Table 1 The five tested perturbation sizes showed a range of behavior

5.2 *Damage modeling results lead to new strength metric*

Local wave interactions in the perturbation region cause tensile stress and damage during the RMI evolution. Fig. 7 shows snapshots in time from a FLAG simulation of damage for $\eta_{0k} = 0.39$. Because the damage study came before the inspection data was examined, all the results in this section come from simulations that used a full sine wave ($q = 1.0$). The contour plot is colored by porosity, also known as void volume fraction, the state variable evolved under tensile stress in the Tonks damage model. Soon after the shock breaks out on the free surface, Fig. 7a, and the perturbations invert, porosity first appears in the subsurface bubble region, Fig. 7b. In shock loading, tensile stresses occur when two or more release waves interact to reduce the pressure below zero. In these RMI experiments, the incident shock reflects off of the free surface and returns into the sample as a release wave. The curvature near the high-points of the initial perturbation, see Fig. 7a, focuses the reflections subsurface, giving rise to tension in the region that becomes the bubble and the porosity predicted there in Fig. 7b. Such porosity decreases the local impedance causing further

release waves, which perturb the stress state elsewhere. Fig. 7c shows that another porosity region later develops below the spike. Fig. 7d show that the more global interaction of the release wave from the free surface with release behind the Taylor wave of the HE shock causes a continuous damage layer and eventually the spall of a layer off the free surface. The global spall occurs well after the spike growth and arrest behavior and so does not concern us.

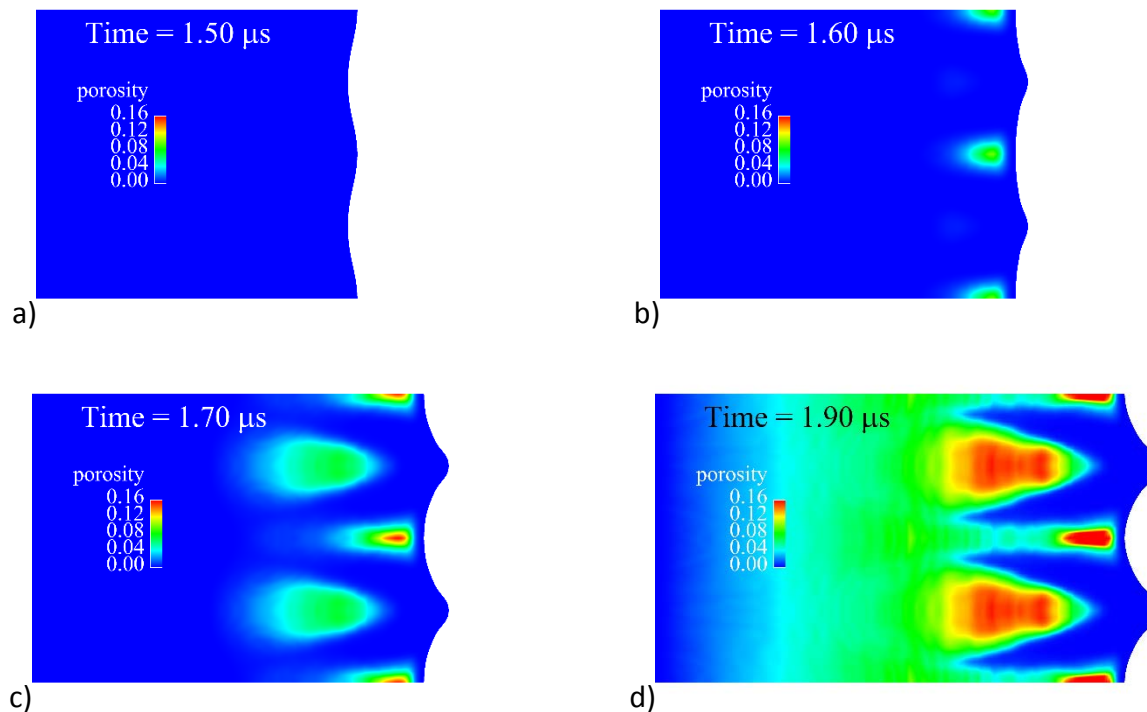


Fig. 7 Porosity predictions from the Tonks damage model for $\eta_{0k} = 0.39$ show that after a) the initial shock breakout on the free surface, b) tensile damage first appears in the near-surface bubble region and c) later appears further subsurface beneath the spikes before d) a continuous porosity layer is formed further subsurface which will later lead to spall

Fig. 8 plots the corresponding spike and bubble velocities for the simulation of Fig. 7 and for a companion simulation with no damage model. In both simulations, the spike and bubble velocities merge to the same value at late time, indicating arrest of the spike growth consistent with the experimental observations for $\eta_{0k} = 0.39$. With the damage model, the late time velocity is constant in

time because of the macroscopic spall layer. Velocities predicted by the damage and no-damage model first diverge at the bubble, consistent with the porosity prediction in Fig. 7. The effects radiate outward from the porous regions and influence the surface velocity of the spike about $0.05 \mu\text{s}$ later. The total spike growth prior to arrest is determined by the relative velocities of these regions and is, therefore, affected by the damage, adding further uncertainty to previous results that analyzed total spike growth but did not consider damage [8,9,13,17,24].

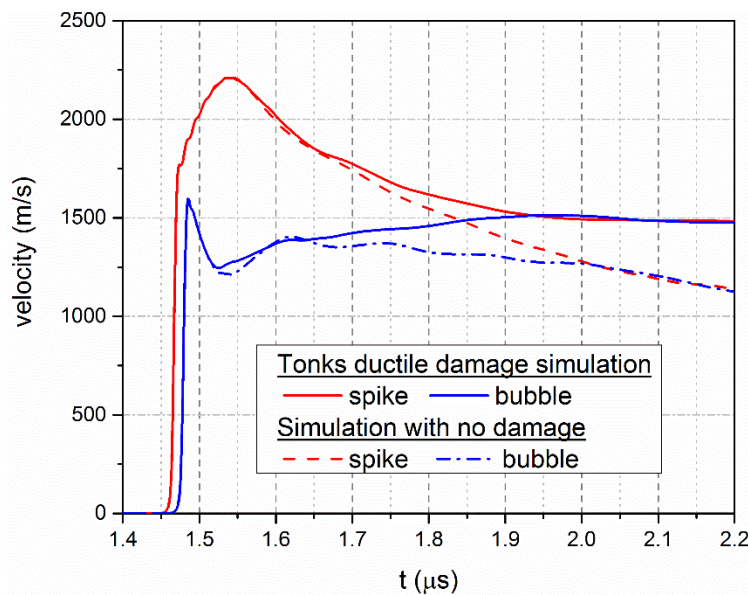


Fig. 8 Tensile damage begins to affect the predicted spike velocity just after the peak velocity, potentially compromising any calculation of total spike growth

The calculation was later repeated on a similar simulation that included the clipped sine wave ($q = 0.55$) for $\eta_{ok} = 0.39$. Without the curvature at the perturbation high points to focus the free-surface release wave, porosity was slightly delayed and amounted to significantly less than in Fig. 7. The effect on velocity and total spike growth was less than Fig. 8 but still noticeable. Since damage still

effects spike growth for this study, and future experiments will have complete sine waves, we will address the issue of damage affecting a strength estimate.

Because of the damage effects, we propose peak spike velocity as a new experimental metric for estimating strength from free-surface RMI experiments. Strength estimates require comparison to a model, so the modeling must be accurate. Damage modeling in these dynamic regimes is notoriously difficult, so we prefer a metric that is untainted by damage effects. Our simulations, including Fig. 8, show that damage does not affect the spike velocity until after the spike velocity begins receding from its peak. Furthermore, from a series of simulations for $\eta_0 k = 0.39$ with a model run with different values of the constant yield strength Y , Fig. 9 shows that the peak spike velocity is quite sensitive to strength.

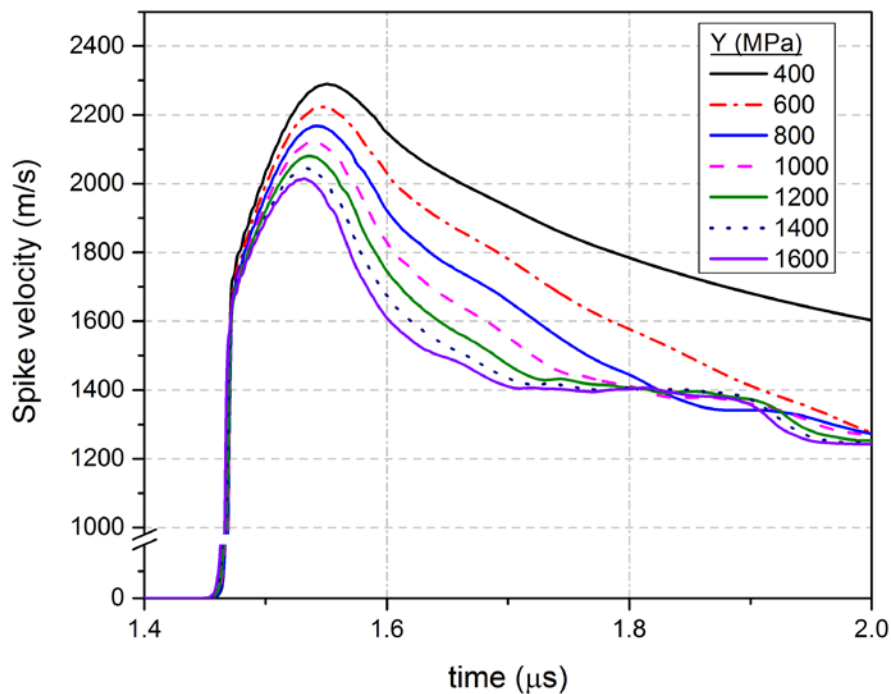


Fig. 9 Simulated spike velocities for $\eta_0 k = 0.39$ show that the peak spike velocity is sensitive to yield strength

Fig. 10 shows an estimated sensitivity, dv_{\max}^s/dY , of peak spike velocity to Y for the perturbations sizes covered by this work and the previous, similar experiments. The sensitivity is taken near $Y = 1000$ MPa from a series of calculations like those for Fig. 9. The sensitivity is sufficient to resolve strength to better than 100 MPa, considering that the peak spike velocities in Table 1 range from 1800 to 2900 m/s and the estimated accuracy of PDV is better than 2%. The sensitivity increases with increasing $\eta_0 k$ as strength plays a more important role in moderating the spike growth, but the effect saturates as the larger spikes become increasingly unstable.

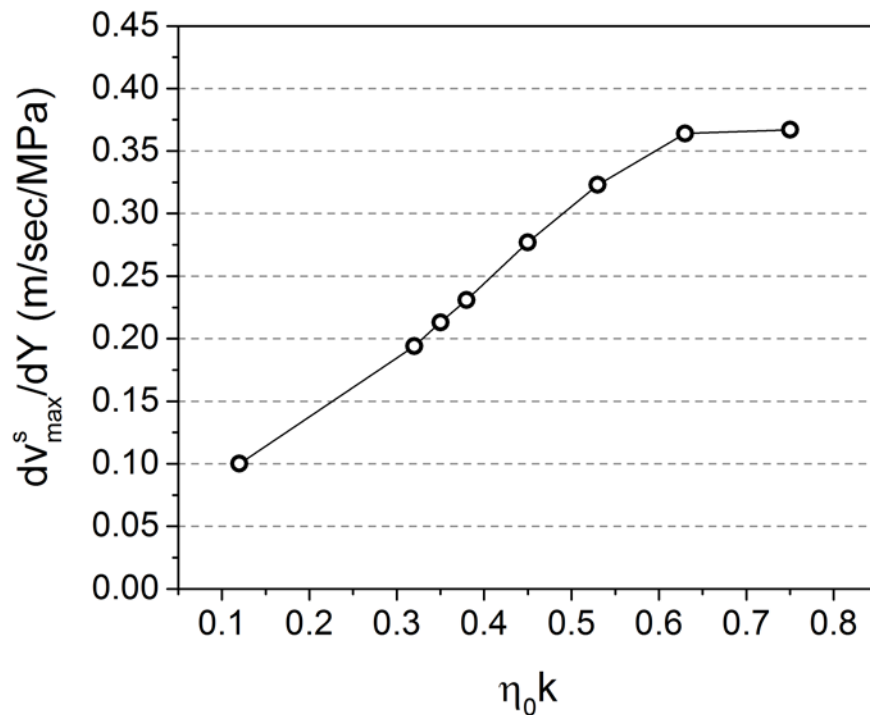


Fig. 10 The sensitivity of the peak spike velocity to changes in yield strength is large enough to estimate strength and increases with increasing initial perturbation size

Peak spike velocity offers additional advantages as a strength metric. We cannot use total spike growth for experiments $\eta_0 k \geq 0.53$ in this work because the spikes did not arrest. We can still use peak spike velocity, and the higher $\eta_0 k$ experiments show greater sensitivity to strength, giving a broader

and better range of experimental data for strength estimation. Peak spike velocity is simpler experimentally because it can be measured without radiography or a measurement of free-surface velocity, one of which is required to determine spike growth. However, a free-surface velocity measurement is still important for validating the modeling of the shock loading.

We cannot conclude that peak spike velocity is always independent of damage. Because release wave speeds do not change, preliminary simulations indicate that geometrically scaling up the experiment causes earlier porosity evolution and might affect the spike velocity prior to the peak. Using impact loading could somewhat delay tension and the resulting porosity because the release wave behind the shock, which also contributes to causing tension, is delayed with a sufficiently thick impactor compared to the release immediately behind the shock with HE loading.

5.3 Convergence and Numerical Viscosity

Numerical convergence must be taken into account to get accurate interpretation of the experimental data, a known issue when modeling RMI [53]. Because the convergence study came before the inspection data was examined, the simulations in this section used a full sine wave ($q = 1.0$). The study also used η_{0k} 's from the previous set of copper experiments. We define "converged" as being sufficiently close (for the purpose at hand) to the value for a hypothetical zone size of zero, determined by extrapolation, which is assumed to be the correct value. Plotting the peak spike velocity versus computational zone size in Fig. 11 for three different sets of simulation shows that the Abaqus results at all mesh sizes are closer to the converged value than are the FLAG calculations. For $\eta_{0k} = 0.32$, the convergence is slightly worse for $Y = 500$ MPa, when the perturbation is somewhat less stable, than for $Y = 1000$ MPa. For $Y = 1000$ MPa, the convergence is worse for $\eta_{0k} = 0.63$, when the

perturbation is significantly less stable than for $\eta_0 k = 0.32$. Encouragingly, the simulations at $\eta_0 k = 0.32$ converge to virtually the same value for both codes, and for $\eta_0 k = 0.63$ the two codes converge to within 1.5% of the same value. Comparing to the converged values for $\eta_0 k = 0.63$, the Abaqus peak velocities were off by -0.7%, -1.5%, and -2.8% for the $3\frac{7}{16}\ \mu\text{m}$, $6\frac{7}{8}\ \mu\text{m}$ and $13\frac{3}{4}\ \mu\text{m}$ zone sizes, respectively. The FLAG with Barton viscosity peak velocities were off by -2.1%, -4.4% and -8.5% for the same zone sizes. Later, we will relate such errors to error magnitude for the strength estimates.

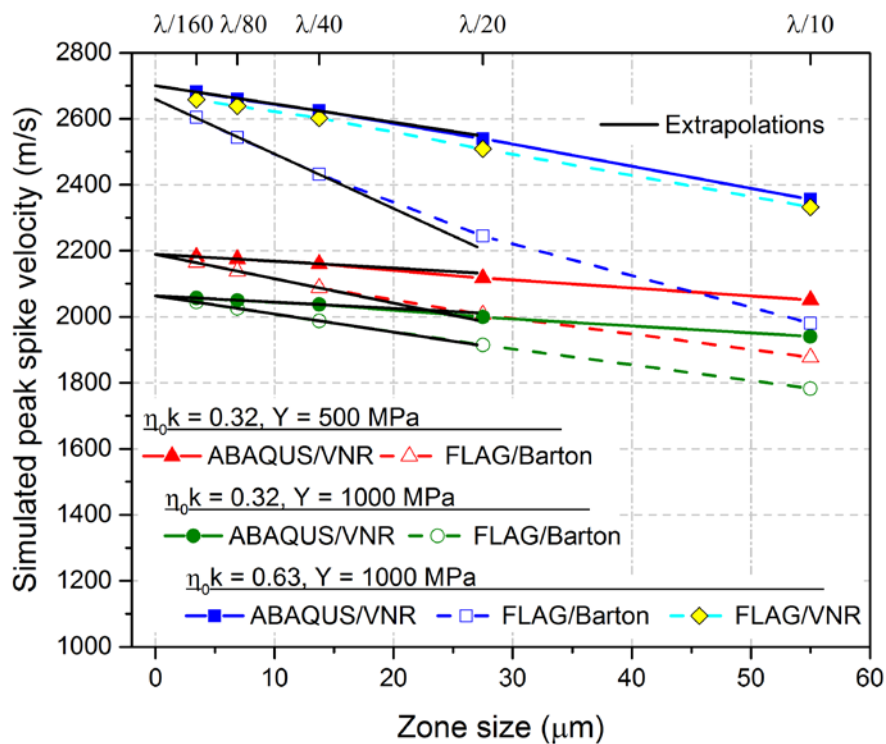


Fig. 11 The peak spike velocities are further from the converged, zero zone size values when Barton numerical viscosity is used rather than VonNeumann and Richtmyer (VNR) viscosity

The significant difference in convergence behavior between the two codes was traced back to differences in numerical viscosity. The post-shock deformation of the instabilities is primarily incompressible plasticity, so the VNR viscosity in Abaqus Explicit adds virtually no dissipation to those deformations. The directional Barton viscosity in FLAG, on the other hand, still provides dissipative

forces. As shown in Fig. 11, we repeated the calculation $\eta_{0k} = 0.63$ in FLAG using a VNR viscosity model and found convergence behavior virtually identical to Abaqus Explicit. Although the VNR model performs better in this particular situation, in general shock problems it can cause non-physical forces transverse to the shock direction and mesh imprinting for shocks that are not aligned with the mesh. In the simulations in this paper, the shock direction, dominant flow direction and mesh lines all coincide well, and the VNR model performs well.

For comparison to data for estimation of strength, the VNR model in FLAG will be used, and the simulated peak velocities for all simulations will be repeated for multiple zone sizes and extrapolated to the zero zone-size converged value. We chose a linear extrapolation based on the best fit to the results from the three smallest zone sizes. Higher order extrapolations proved to be less stable because of noise in the peak velocities caused by some artificial ringing from the shock.

5.4 Effect of Incomplete Sine Waves

The flattened tops on the initial perturbations, shown in Fig. 3 and defined in Eq. 1, have a significant effect on the calculated peak spike velocity. Fig. 12 shows the converged peak spike velocity for simulations for varying degrees of the completeness of the initial sine wave for a test case of $\eta_{0k} = 0.44$ and $Y = 600$ MPa. Combining the numbers from Fig. 12 with those from Fig. 10, a change in q of 0.1 is roughly equivalent to a change in Y of 100–300 MPa. Therefore, the as-built geometry must be modeled in order to get an accurate estimate of strength.

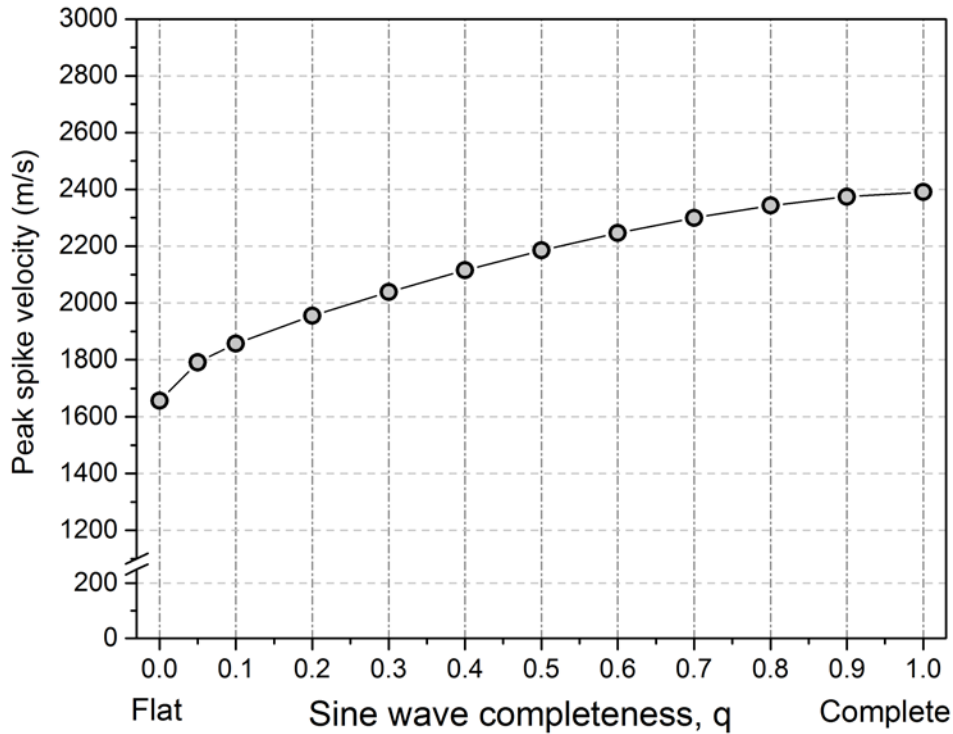


Fig. 12 The flattened tops on the initial perturbations, shown in **Fig. 3** and defined in Eq. 1, have a significant effect on the calculated peak spike velocity. Calculated for $\eta_{ok} = 0.44$ and $Y = 600$ MPa

The results in Fig. 12 are somewhat surprising. Even for a q of 0.9 or 0.8, only 10% or 20% clipping of the sine-wave peaks, the effect on peak spike velocity is significant and measurable. Because the (clipped) initial peaks become the bubbles after inversion, see Fig. 2, and we are measuring the peak velocity at the spike, we did not intuitively predict the clipping to affect our metric. However, the effect is plausible. Since the spike and the bubble are separated by about $\lambda/2$, or 0.275 mm, and the sound speed of copper is about 4 mm/ μ s, the two regions could “communicate” in about 0.07 μ s. Referring to Fig. 8, the peak spike velocity occurs more than 0.1 μ s after the clipped region of the bubble is shocked, so there is time for the clipped region to affect the peak spike velocity.

5.5 *Strength Estimate*

Based on the studies detailed above, the VNR viscosity model in FLAG was used for strength estimates, and the simulated peak velocities for all simulations were repeated for multiple zone sizes and extrapolated to the zero zone-size converged value. The simulations used as-built geometries with the clipped sine waves as given in Table 1.

Fig. 13 shows the error between the measured peak spike velocities for all 5 η_{ok} 's and the calculations plotted versus the yield strength in the calculations. The results are interpolated to estimate $Y = 530$ MPa as giving zero mean error. This estimate agrees well with the minimum in the root-mean square error, which is harder to interpolate precisely from the limited points. The minima in RMS error of about 12 m/s is modestly smaller than the uncertainties estimated at 20-30 m/s for the data, see Table 1. We heuristically assign an uncertainty of ± 100 MPa to our strength estimate based on the breadth of the minimum in the plot of root-mean-square (RMS) error and the uncertainties in the geometry and the extracted peak velocities. Although ± 100 MPa might be a conservative estimate of random uncertainties, it potentially underestimates uncertainties from bias errors such as inaccuracies in modeling the high-explosive pressure load. For reference, similar calculations using the less-convergent Barton viscosity give an estimate of $Y = 490$ MPa, which is reasonable agreement considering the uncertainty in extrapolating to zero zone-size.

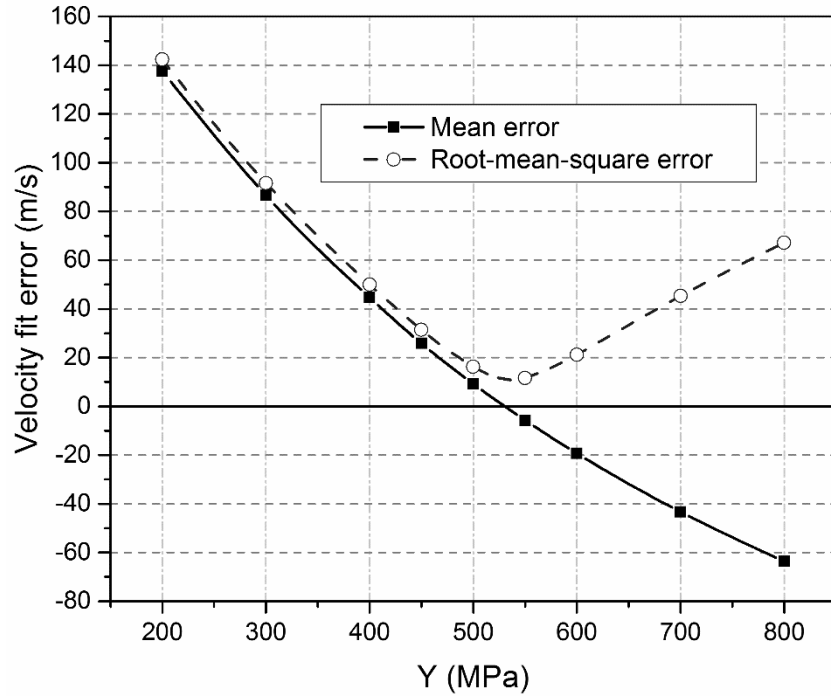


Fig. 13 The minimum of the root-mean-square errors between the measured peak spike velocities and the converged calculational values reveal the best estimate of strength

Fig. 14 shows the predicted, converged peak velocities for the estimated strength value compared to the experimental data from Table 1. Uncertainty bounds correspond to the ± 100 MPa in the strength estimates. The model agrees quite well with the full suite of experiments.

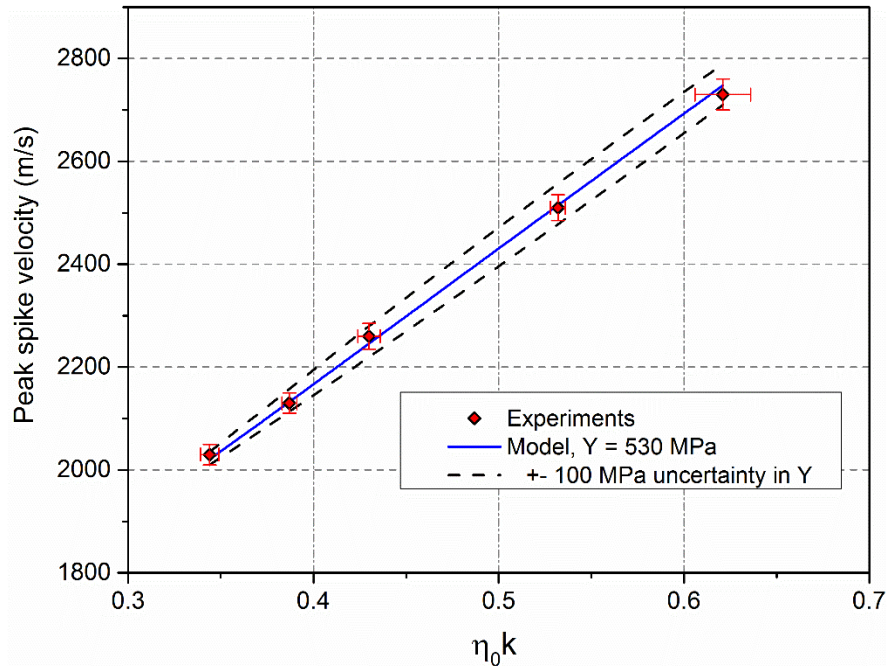


Fig. 14 An average strength of 530 ± 100 MPa in the numerical model fit the full set of experimental data well

Previously published strength estimates [8,9,13,24] for the same copper from the previous RMI experiments [9] were all based on the assumption of complete sine waves. Based on the sensitivity shown in Fig. 12 to the clipped sine waves, the previous estimates should be considered significantly uncertain. The previous estimates also used the total spike growth metric and were based on Lagrangian simulations for an internal surface perturbation [6] not a free surface perturbation, so any similarity of the strength estimates might be caused by compensating effects.

Using under-converged modeling would result in significantly underestimating strength. We repeated the strength estimate using the calculated peak spike velocities for the three finest calculational zone sizes rather than converged values and using both viscosity models in FLAG. Fig. 15 shows the resulting strength estimates as a function of zone size, with the converged results plotted at a zone size of zero. The variation of the estimated strength with zone size can be significant. For the zone size of $3^{7/16} \mu\text{m}$ or $\lambda/160$ the VNR-based estimate only differs from the converged estimate by 40

MPa, but the Barton-based estimate already differs by 160 MPa. Even for the better-converged VNR viscosity, the estimate differs from the converged estimate by 160 MPa when the zone size reaches $13\frac{3}{4}\ \mu\text{m}$ or $\lambda/40$. The surprising sensitivity occurs because the convergence rates taken as the slopes from Fig. 11 would be divided by the sensitivities in Fig. 10, relatively small numbers, to get the sensitivity of the strength estimate to zone size. A previously reported estimate of 520 MPa strength for one of these experiments was based on FLAG/Barton calculation with $20\ \mu\text{m}$ zoning [24], and should have significantly underestimated the strength, but that experiment potentially also had incomplete sine-wave perturbations that were not modeled. An RMI-based strength estimate in cerium used FLAG/Barton and $10\ \mu\text{m}$ zoning [18] and therefore probably significantly underestimated the strength.

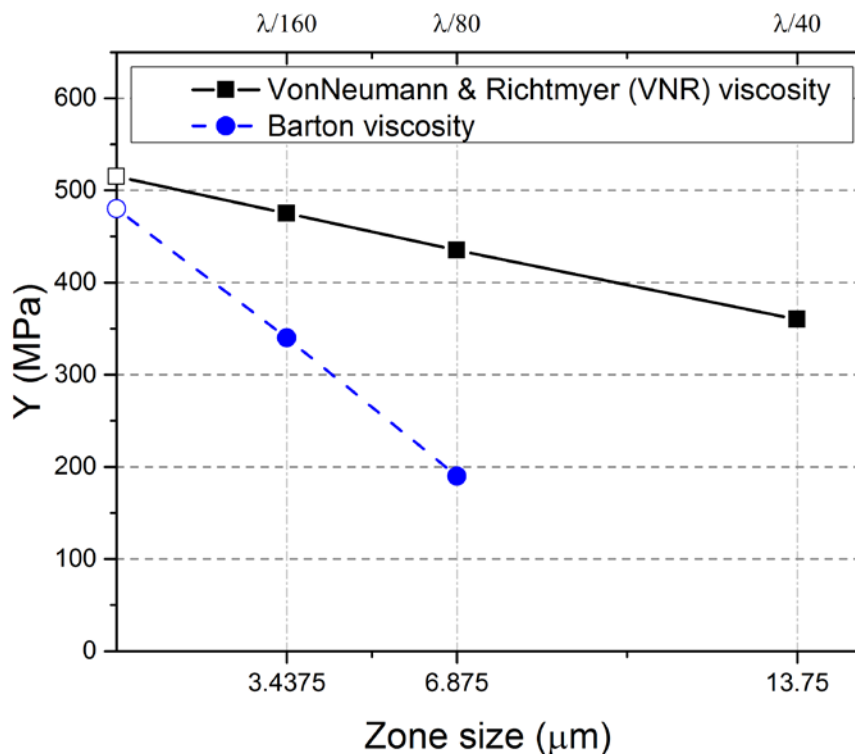


Fig. 15 Mesh size convergence effects can result in significantly underestimating the yield strength, especially using a Barton numerical viscosity model. The open symbols indicate an estimate based on extrapolation to zero zone size

That the zone sizes in Fig. 15 are all smaller than the copper's grain size of about 20 μm should not necessarily cause concern. The issues of numerical convergence and assuming a homogeneous continuum are critical considerations but are largely independent. In the calculations, we use discretization to approximate the exact solution to a set of differential equations over some geometric domain. As Fig. 11 and Fig. 15 show, the convergence of the numerical solution depends on the method of solution and might or might not require discretization that turns out to be smaller than the physical grain size. Even though the FLAG/Barton calculations require finer zoning to achieve the same convergence, all the calculations show well-behaved convergence and converge to acceptably close final results. Although one should be wary when a solution requires especially fine discretization, the grain size cannot be justified as a final arbiter of acceptable zoning. A prediction of sub-grain size features would be a cause for concern but was not observed in any simulations in this work.

On the other hand, assuming an isotropic, homogeneous continuum must be justified whether or not we solve some problem exactly or via numerical discretization. In the experiment, the perturbation wavelengths are about 28 times the grain size although the perturbation amplitudes are on the order of the grain size. The PDV laser spot size of about 1 mm diameter views thousands of surface grains, and their kinematic behavior is influenced by the subsurface grains as well, all of which supports assuming a homogeneous continuum. Although it is possible that heterogeneity on scale of the grain size contribute to stochasticity in the experimental results, we suspect that other experimental limitations are more significant. The assumption of isotropic behavior is justified because this copper source is used extensively at Los Alamos has been shown to have minimal texture [54,55].

5.6 Heterogeneity of State Variables

To establish the conditions tested by our experiment and to investigate the appropriateness of estimating an *average* strength, we examined the spatial and temporal variations of strain, strain rate, and temperature. Buttler gave analytical approximations for average strains and strain rates based on Piriz's assumptions [9], but those equations are only valid after the peak spike velocity, and we are concerned with the behavior up until the peak since that is our metric for strength. Therefore, we extracted variables from simulations using $Y = 600$ MPa and with the VNR viscosity model that gave better convergence. $6\frac{7}{8}$ μm zoning was used because the relevant quantities were converged to within a few percent, sufficient for the qualitative discussion in the section.

From the spatially heterogeneous fields, we hypothesized that the most relevant state variables for strength were those in the region of the spike that undergoes the most plastic strain. Therefore, we extracted time histories for the computational zone in the spike with the highest value of equivalent plastic strain at the time of peak spike velocity. Fig. 16 shows the equivalent plastic strain rate plotted versus equivalent plastic strain for the minimum, maximum, and two intermediate values of η_{0k} . The two humps at the beginning of each curve are the plastic strain for the shock and release, respectively, and are nearly identical since all regions see the same shock. Because numerical viscosity smears the shock, numerical strain rates in the shock do not converge to a finite value upon mesh refinement and therefore have little significance. The subsequent portions of the curves do converge and reveal the differences in behavior. To mark the time of peak spike velocity, the curves transition to dashed lines. For $\eta_{0k} = 0.34$, the spike sees an additional 25% plastic strain¹ between the shock release and the peak

¹ Buttler et al. [9] estimated the time and spatially averaged plastic strain rate in a spike with $\eta_{0k} = 0.35$ at 1.5×10^7 /s, and also give much higher estimates of plastic strain and temperature. Those estimates were based on the equations of Piriz [6] and used a value of $1/3$ for the constant α . A value of $3/2$ matches the numerical simulations

spike velocity at a rate of just under $6 \times 10^6/s$. At $\eta_{ok} = 0.62$, the spike sees almost 100% additional plastic strain by the time of peak spike velocity, at a rate just over $1 \times 10^7/s$. Considering that strength is generally dependent on the logarithm of the strain rate, e.g., [51], the range of strain rates covered by the different η_{ok} 's is modest. Therefore, one might reasonably approximate the set of experiments as probing a common strain rate. The calculated temperatures, including both residual heating from the shock and plastic work, in these zones at the time of peak spike velocity are 475K, 506K, 562K and 586K for $\eta_{ok} = 0.34, 0.43, 0.53$ and 0.62 . Considering that all of the copper is heated to approximately 400K by the shock and release, the temperature ranges are also relatively modest.

here, and is consistent with more recent work [56][57]. Switching to $\alpha = 3/2$ in the equations in Buttler reduces the strain rate and strain estimates by about one order of magnitude [58].

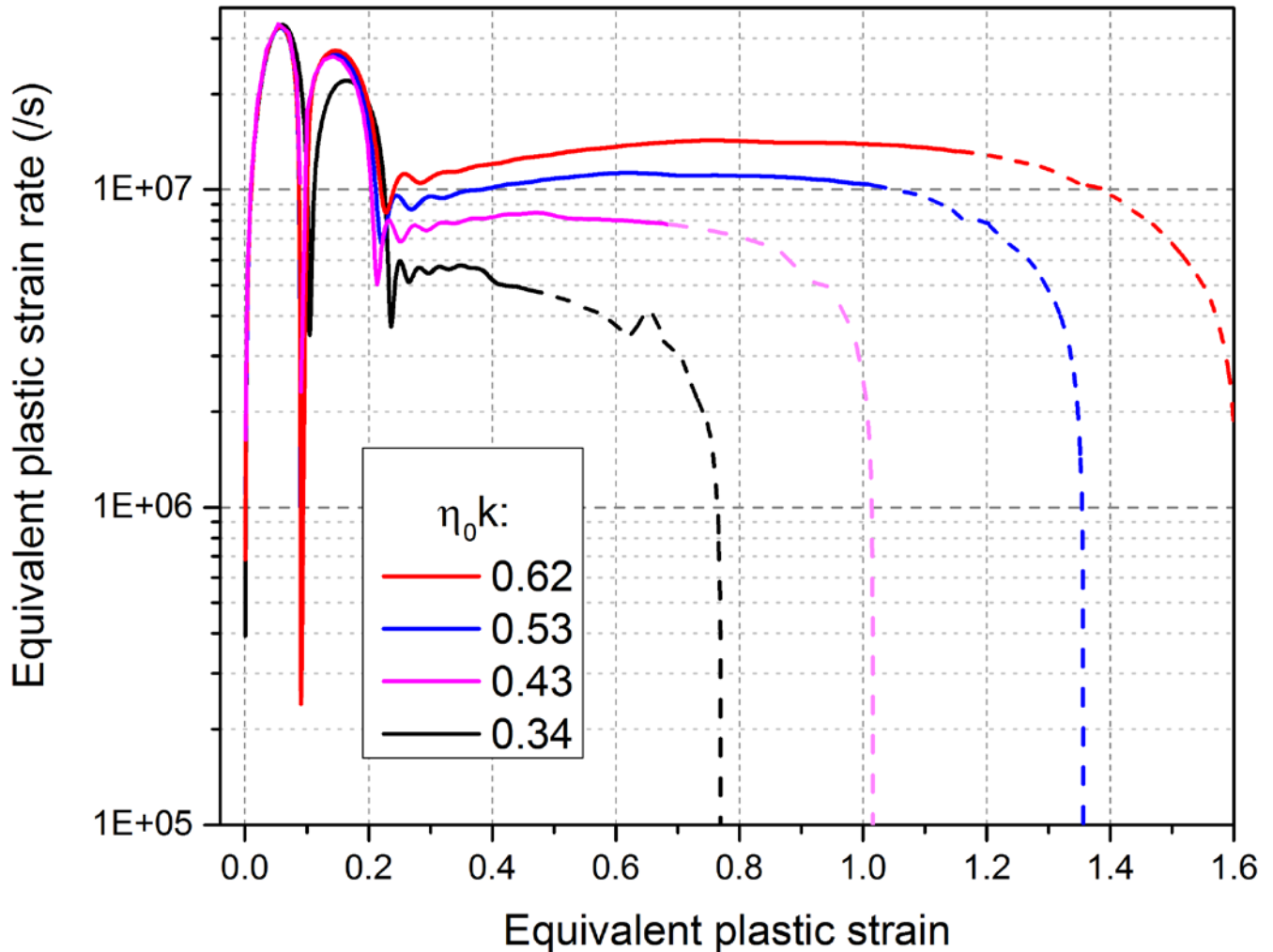


Fig. 16 Plastic strain versus strain rate for the computation zones in the spike with the highest peak plastic strain. The curves are dashed for time after the peak spike velocity since the strength estimate is not affected by behavior after the peak

As in past work [24], we propose that the estimated RMI strength result be used as a single yield-strength value at the appropriate strain, rate and temperature for calibrating a strength model along with a broader set of quasi-static and Hopkinson bar data. Note that the strength estimate represents the post-shock state of the material, which must be taken into account [59]. Because of the dearth of data at rates above $10^4/s$, the single average strength number is quite valuable for constraining the calibration. More sophisticated treatments are left to future work.

6 Conclusions and Future Work

Based on new experimental data and a new analysis procedure, we find that free-surface Richtmyer-Meshkov Instability (RMI) experiments can sensitively estimate deviatoric strength of metals at strain rates up to at least $10^6/s$ to $10^7/s$. Strength measurement at such rates is very difficult, and RMI complements existing approaches and significantly expands the general capability.

Our results demonstrate that a new experimental metric provides several advantages for estimating strength from RMI experiments. In free-surface RMI experiments, tensile stresses can cause damage that will affect the growth and arrest of the perturbations. For the copper RMI experiments examined in this paper, we found that using peak spike velocity as an experimental metric instead of total spike growth allowed us to avoid the corrupting effects of damage. In general, peak spike velocity shows good sensitivity to strength and, compared to using total spike growth, allows the extraction of strength from experiments at higher $\eta_0 k$ (bigger initial perturbations) that go unstable. Higher $\eta_0 k$ experiments are advantageous because they are even more sensitive to strength and exercise higher strains and strain rates. Furthermore, using peak spike velocity as the metric removes any need for radiography and thus makes for significantly simpler experiments, and velocity can generally be measured more accurately and precisely than radiographic quantities.

Our results also show the benefit of using a range of $\eta_0 k$ data to estimate an average strength. Trying to fit our full data set with a consistent strength estimate forced us to examine our Lagrangian hydrodynamic modeling in more detail. We found that mesh under-convergence resulted in underestimating strength, so we extrapolated our numerical estimates to a converged value. Using classic VonNeumann and Richtmyer numerical viscosity improved the mesh convergence over a Barton approach for this simulation but might reduce fidelity in more shock-dominated problems. Using the

full range of η_{ok} data also allowed us to make a more confident strength estimate with a more realistic uncertainty estimate. For the half-hard copper in this study, we estimated an average strength of 530 \pm 100 MPa at strain rates between $2 \times 10^6/s$ and $1.6 \times 10^7/s$.

For future experiments, impact loading would have advantages over high explosive (HE) loading. Impact loading is much easier to model accurately since the shock pressure is determined just by the impact velocity, which can be measured accurately, and Hugoniot of the impactor and target rather than by HE modeling issues and the details of the decay of the Taylor wave in the sample. Accurate modeling of the pressures and stresses driving the instabilities is crucial for accurate strength estimates. Impact loading additionally provides some delay in tensile damage because of the flat-top pressure wave compared the HE Taylor wave that starts releasing immediately behind the peak. Impact experiments are also usually easier to field.

We could probably learn more about strength by expanding to the experimental space beyond varying only η_{ok} to include varying impact pressures, size scales or starting temperature. A suitable set of experiments and/or a more sophisticated analysis might reveal something about the dependence of strength on strain, strain rate or temperature. An even more ambitious study could include testing the same material using multiple high-rate strength platforms such as RMI, Rayleigh-Taylor, and wave profile analysis from high pressure experiments [60-62], and then comparing the strength estimates and investigating any differences.

Table 2 gives a brief comparison of instability-based approaches for estimating high-rate material strength. The free-surface RMI experiments described here are probably the easiest to field and diagnose. They seem to interrogate strength at higher strain rates than Rayleigh-Taylor experiments, but a more objective way to quantify spatially and temporally varying rates is needed for

a fair comparison [9]. The free-surface RMI experiments probe strength at low pressures. Rayleigh-Taylor and internal-perturbation RMI experiments offer the ability to probe strength at high pressure, but they currently require radiographic interrogation.

	Rayleigh-Taylor	Richtmyer-Meshkov Internal Perturbations	Richtmyer-Meshkov Free Surface
Acceleration	Shockless	Shock	Shock
Strain rate	High	High	High
Pressure	High (confined)	High (confined)	Low (free surface releases)
Main diagnostic	Radiography	Radiography	Surface velocimetry
Measured behavior	Growth rate	Arrest – final spike height	Peak spike velocity

Table 2 Comparing different types of dynamic instability-based experiments that can be used to infer strength at very high rates

7 Acknowledgements

Los Alamos National Laboratory, an affirmative action/equal opportunity employer, is operated by the Los Alamos National Security, LLC for the National Nuclear Security Administration of the U.S. Department of Energy under contract DE-AC52-06NA25396. By approving this article, the publisher recognizes that the U.S. Government retains nonexclusive, royalty-free license to publish or reproduce the published form of this contribution, or to allow others to do so, for U.S. Government purposes. Los Alamos National Laboratory strongly supports academic freedom and a researcher's right to publish; as an institution, however, the Laboratory does not endorse the viewpoint of a publication or guarantee its technical correctness.

8 References

1. Barnes JF, Blewett PJ, McQueen RG, Meyer KA, Venable D (1974) Taylor instability in solids. *J Appl Phys* 45 (2):727-732. doi:doi:<http://dx.doi.org/10.1063/1.1663310>

2. Colvin JD, Legrand M, Remington BA, Schurtz G, Weber SV (2003) A model for instability growth in accelerated solid metals. *J Appl Phys* 93 (9):5287-5301. doi:doi:<http://dx.doi.org/10.1063/1.1565188>
3. Lebedev AI, Nizovtsev PN, Rayevsky VA, Solovyov VP Rayleigh–Taylor Instability in Strong Media, Experimental Study. Young R, Glimm J, Boston B (eds) *Proceedings of the Fifth International Workshop on Compressible Turbulent Mixing*, 1996.
4. Barton NR, Bernier JV, Becker R, Arsenlis A, Cavallo R, Marian J, Rhee M, Park H-S, Remington BA, Olson RT (2011) A multiscale strength model for extreme loading conditions. *J Appl Phys* 109 (7):073501. doi:doi:<http://dx.doi.org/10.1063/1.3553718>
5. Smith RF, Eggert JH, Rudd RE, Swift DC, Bolme CA, Collins GW (2011) High strain-rate plastic flow in Al and Fe. *J Appl Phys* 110 (12):123515. doi:doi:<http://dx.doi.org/10.1063/1.3670001>
6. Piriz AR, Cela J, Tahir NA, Hoffmann DHH (2008) Richtmyer-Meshkov instability in elastic-plastic media. *Phys Rev E* 78 (5):056401
7. Piriz AR, Cela J, Tahir NA (2009) Richtmyer–Meshkov instability as a tool for evaluating material strength under extreme conditions. *Nucl Instrum Meth A* 606 (1):139-141
8. Dimonte G, Terrones G, Cherne FJ, Germann TC, Dupont V, Kadau K, Buttler WT, Oro DM, Morris C, Preston DL (2011) Use of the Richtmyer-Meshkov instability to infer yield stress at high-energy densities. *Phys Rev Lett* 107 (26):264502
9. Buttler WT, Oró DM, Preston DL, Mikaelian KO, Cherne FJ, Hixson RS, Mariam FG, Morris C, Stone JB, Terrones G, Tupa D (2012) Unstable Richtmyer-Meshkov growth of solid and liquid metals in vacuum. *J Fluid Mech* 703:60-84
10. López Ortega A, Lombardini M, Pullin DI, Meiron DI (2014) Numerical simulations of the Richtmyer-Meshkov instability in solid-vacuum interfaces using calibrated plasticity laws. *Phys Rev E* 89 (3):033018
11. Mikaelian KO (2013) Shock-induced interface instability in viscous fluids and metals. *Phys Rev E* 87 (3):031003
12. Plohr JN, Plohr BJ (2005) Linearized analysis of Richtmyer-Meshkov flow for elastic materials. *J Fluid Mech* 537:55-89
13. Prime MB, Vaughan DE, Preston DL, Buttler WT, Chen SR, Oró DM, Pack C (2014) Using growth and arrest of Richtmyer-Meshkov instabilities and Lagrangian simulations to study high-rate material strength. *Journal of Physics: Conference Series* 500 (11):112051
14. Opie S, Gautam S, Fortin E, Lynch J, Peralta P, Loomis E (2016) Behaviour of rippled shocks from ablatively-driven Richtmyer-Meshkov in metals accounting for strength. *Journal of Physics: Conference Series* 717 (1):012075
15. John KK (2014) Strength of tantalum at high pressures through Richtmyer-Meshkov laser compression experiments and simulations. Ph.D. Dissertation, California Institute of Technology, Pasadena, CA
16. Sternberger Z, Ravichandran R, Wehrenberg C, Remington B, Maddox B, Opachich K, Randall G, Farrell M A comparative study of Rayleigh-Taylor and Richtmyer-Meshkov instabilities in 2D and 3D in tantalum. to appear, *APS Shock Compression of Condensed Matter Conference Proceedings*, 2015. p 4003
17. Buttler WT, Oro DM, Preston D, Mikaelian KO, Cherne FJ, Hixson RS, Mariam FG, Morris CL, Stone JB, Terrones G, Tupa D (2012) The study of high-speed surface dynamics using a pulsed proton beam. *AIP Conference Proceedings* 1426 (1):999-1002. doi:doi:<http://dx.doi.org/10.1063/1.3686446>

18. Jensen BJ, Cherne FJ, Prime MB, Fezzaa K, Iverson AJ, Carlson CA, Yeager JD, Ramos KJ, Hooks DE, Cooley JC, Dimonte G (2015) Jet formation in cerium metal to examine material strength. *J Appl Phys* 118 (19):195903. doi:doi:<http://dx.doi.org/10.1063/1.4935879>
19. Asay JR, Mix LP, Perry FC (1976) Ejection of material from shocked surfaces. *Applied Physics Letters* 29 (5):284-287. doi:doi:<http://dx.doi.org/10.1063/1.89066>
20. Germann TC, Hammerberg JE, Holian BL (2004) Large-Scale Molecular Dynamics Simulations of Ejecta Formation in Copper. *AIP Conference Proceedings* 706 (1):285-288. doi:doi:<http://dx.doi.org/10.1063/1.1780236>
21. Zellner MB, Buttler WT (2008) Exploring Richtmyer–Meshkov instability phenomena and ejecta cloud physics. *Applied Physics Letters* 93 (11):114102. doi:doi:<http://dx.doi.org/10.1063/1.2982421>
22. Zellner MB, Dimonte G, Germann TC, Hammerberg JE, Rigg PA, Stevens GD, Turley WD, Buttler WT (2009) Influence of shockwave profile on ejecta. *AIP Conference Proceedings* 1195 (1):1047-1050. doi:doi:<http://dx.doi.org/10.1063/1.3294980>
23. Dimonte G, Terrones G, Cherne FJ, Ramaprabhu P (2013) Ejecta source model based on the nonlinear Richtmyer–Meshkov instability. *J Appl Phys* 113 (2):024905. doi:doi:<http://dx.doi.org/10.1063/1.4773575>
24. Prime MB, Buttler WT, Sjue SK, Jensen BJ, Mariam FG, Oró DM, Pack CL, Stone JB, Tupa D, Vogan-McNeil W (2016) Using Richtmyer–Meshkov Instabilities to Estimate Metal Strength at Very High Rates. Song B, Lamberson L, Casem D, Kimberley J (eds) *Dynamic Behavior of Materials, Volume 1*. Conference Proceedings of the Society for Experimental Mechanics Series. Springer International Publishing, pp 191-197. doi:10.1007/978-3-319-22452-7_27
25. King NSP, Ables E, Adams K, Alrick KR, Amann JF, Balzar S, Barnes Jr PD, Crow ML, Cushing SB, Eddleman JC (1999) An 800-MeV proton radiography facility for dynamic experiments. *Nucl Instrum Meth A* 424 (1):84-91
26. Holtkamp DB Survey of optical velocimetry experiments-applications of PDV, a heterodyne velocimeter. Kiuttu GF, Turchi PJ, Reinovsky RE (eds) *2006 International Conference on Megagauss Magnetic Field Generation and Related Topics*, Santa Fe, NM, 2006. IEEE, pp 119-128. doi:10.1109/MEGAGUSS.2006.4530668
27. Yeh Y, Cummins HZ (1964) Localized Fluid Flow Measurements with nn He–Ne Laser Spectrometer. *Applied Physics Letters* 4 (10):176-178. doi:doi:<http://dx.doi.org/10.1063/1.1753925>
28. Foreman JW, George EW, Lewis RD (1965) Measurement of Localized Flow Velocities in Gases with a Laser Doppler Flowmeter. *Applied Physics Letters* 7 (4):77-78. doi:doi:<http://dx.doi.org/10.1063/1.1754319>
29. Buttler WT, Lamoreaux SK, Omenetto FG, Torgerson JR (2004) Optical Velocimetry. *ArXiv Physics e-prints*
30. Strand OT, Goosman DR, Martinez C, Whitworth TL, Kuhlrow WW (2006) Compact system for high-speed velocimetry using heterodyne techniques. *Review of Scientific Instruments* 77 (8):083108. doi:doi:<http://dx.doi.org/10.1063/1.2336749>
31. Caramana EJ, Burton DE, Shashkov MJ, Whalen PP (1998) The Construction of Compatible Hydrodynamics Algorithms Utilizing Conservation of Total Energy. *J Comput Phys* 146 (1):227-262. doi:<http://dx.doi.org/10.1006/jcph.1998.6029>
32. Burton DE, Carney TC, Morgan NR, Runnels SR, Sambasivan SK, Shashkov MJ (2011) A cell-centered Lagrangian hydrodynamics method for multi-dimensional unstructured grids in curvilinear coordinates with solid constitutive models. Los Alamos National Laboratory Report Report LA-UR-11-04995

33. Kenamond M, Bement M, Shashkov M (2014) Compatible, total energy conserving and symmetry preserving arbitrary Lagrangian–Eulerian hydrodynamics in 2D rz – Cylindrical coordinates. *J Comput Phys* 268:154-185. doi:<http://dx.doi.org/10.1016/j.jcp.2014.02.039>
34. Burton DE (1992) Connectivity structures and differencing techniques for staggered-grid free-Lagrange hydrodynamics. Report Lawrence Livermore National Laboratory, Report No. UCRL–JC–110555
35. Burton DE (1994) Consistent Finite-Volume Discretization of Hydrodynamic Conservation Laws for Unstructured Grids. Lawrence Livermore National Laboratory Report UCRL–JC–118788.
36. Fung J, Harrison AK, Chitanvis S, Margulies J (2013) Ejecta source and transport modeling in the FLAG hydrocode. *Computers & Fluids* 83:177-186. doi:<http://dx.doi.org/10.1016/j.compfluid.2012.08.011>
37. Sambasivan SK, Shashkov MJ, Burton DE (2013) A finite volume cell-centered Lagrangian hydrodynamics approach for solids in general unstructured grids. *International Journal for Numerical Methods in Fluids* 72 (7):770-810. doi:10.1002/flid.3770
38. Morgan NR, Kenamond MA, Burton DE, Carney TC, Ingraham DJ (2013) An approach for treating contact surfaces in Lagrangian cell-centered hydrodynamics. *J Comput Phys* 250:527-554. doi:<http://dx.doi.org/10.1016/j.jcp.2013.05.015>
39. Denissen NA, Rollin B, Reisner JM, Andrews MJ (2014) The Tilted Rocket Rig: A Rayleigh–Taylor Test Case for RANS Models1. *Journal of Fluids Engineering* 136 (9):091301-091301. doi:10.1115/1.4027776
40. Lipnikov K, Reynolds J, Nelson E (2013) Mimetic discretization of two-dimensional magnetic diffusion equations. *J Comput Phys* 247:1-16. doi:<http://dx.doi.org/10.1016/j.jcp.2013.03.050>
41. Simulia Abaqus 6.14 (2014). Dassault Systems,
42. Landshoff R (1955) A numerical method for treating fluid flow in the presence of shocks. Los Alamos National Laboratory Report LA-1930
43. VonNeumann J, Richtmyer RD (1950) A Method for the Numerical Calculation of Hydrodynamic Shocks. *J Appl Phys* 21 (3):232-237. doi:<http://dx.doi.org/10.1063/1.1699639>
44. Margolin LG (1988) A centered artificial viscosity for cells with large aspect ratio. Report Lawrence Livermore National Laboratory report UCRL-53882
45. Steinberg DJ (1996) Equation of State and Strength Properties of Selected Materials. Lawrence Livermore National Laboratory Report UCRL-MA-106439 Change 1
46. Tonks D, Zurek A, Thissell W, Vorthman J, Hixson R (2002) The Tonks ductile damage model. Los Alamos National Laboratory Report LA-UR-03-0809
47. Zurek AK, Thissell WR, Johnson JN, Tonks DL, Hixson R (1996) Micromechanics of spall and damage in tantalum. *Journal of Materials Processing Technology* 60 (1–4):261-267. doi:[http://dx.doi.org/10.1016/0924-0136\(96\)02340-0](http://dx.doi.org/10.1016/0924-0136(96)02340-0)
48. Tonks DL (1994) Percolation wave propagation, and void link-up effects in ductile fracture. *Le Journal de Physique IV* 4 (C8):C8-665-C668-670
49. Tonks DL, Zurek AK, Thissell WR (2002) Void Coalescence Model for Ductile Damage. *AIP Conference Proceedings* 620 (1):611-614. doi:<http://dx.doi.org/10.1063/1.1483613>
50. Tonks DL, Bronkhorst CA, Bingert JF (2011) Inertial Effects In Dynamical Ductile Damage in Copper. Los Alamos National Laboratory Report LA-UR-11-05803
51. Preston DL, Tonks DL, Wallace DC (2003) Model of plastic deformation for extreme loading conditions. *J Appl Phys* 93 (1):211-220

52. Dobratz BM, Crawford PC (1985) LLNL Explosives Handbook. Properties of chemical explosives and explosive simulants. Lawrence Livermore National Laboratory Report UCRL-52997 Change 2
53. López Ortega A, Lombardini M, Barton PT, Pullin DI, Meiron DI (2015) Richtmyer–Meshkov instability for elastic–plastic solids in converging geometries. *Journal of the Mechanics and Physics of Solids* 76:291-324. doi:<http://dx.doi.org/10.1016/j.jmps.2014.12.002>
54. Escobedo JP, Dennis-Koller D, Cerreta EK, Patterson BM, Bronkhorst CA, Hansen BL, Tonks D, Lebensohn RA (2011) Effects of grain size and boundary structure on the dynamic tensile response of copper. *J Appl Phys* 110 (3):033513. doi:10.1063/1.3607294
55. Bodelot L, Escobedo-Diaz JP, Trujillo CP, Martinez DT, Cerreta EK, Gray Iii GT, Ravichandran G (2015) Microstructural changes and in-situ observation of localization in OFHC copper under dynamic loading. *International Journal of Plasticity* 74:58-74. doi:<http://dx.doi.org/10.1016/j.ijplas.2015.06.002>
56. Piriz AR, Sun YB, Tahir NA (2015) Hydrodynamic instability of elastic-plastic solid plates at the early stage of acceleration. *Phys Rev E* 91 (3):033007
57. Piriz AR, private communication, 14 March 2016.
58. Preston DL, private communication, 1 May 2015.
59. Meyers MA (1994) *Dynamic behavior of materials*. John Wiley & sons,
60. Asay JR, Lipkin J (1978) A self-consistent technique for estimating the dynamic yield strength of a shock-loaded material. *Journal of Applied Physics* 49 (7):4242-4247. doi:<http://dx.doi.org/10.1063/1.325340>
61. Brown JL, Alexander CS, Asay JR, Vogler TJ, Ding JL (2013) Extracting strength from high pressure ramp-release experiments. *Journal of Applied Physics* 114 (22):223518. doi:<http://dx.doi.org/10.1063/1.4847535>
62. Reinhart WD, Asay JR, Alexander CS, Chhabildas LC, Jensen B (2015) Flow Strength of 6061-T6 Aluminum in the Solid, Mixed Phase, Liquid Regions. *Journal of Dynamic Behavior of Materials* 1 (3):275-289. doi:10.1007/s40870-015-0030-6